Probing nanomechanics by direct indentation using Nanoendoscopy-AFM reveals the nuclear elasticity transition in cancer cells.

Takehiko Ichikawa[1]*, Yohei Kono[1], Makiko Kudo[1], Takeshi Shimi[1], Naoyuki Miyashita[2], Tomohiro Maesaka[2], Kojiro Ishibashi[3], Takeshi Yoshida[1,4], Kundan Sivashanmugan[5], Rikinari Hanayama[1,4], Eishu Hirata[1,3], Kazuki Miyata[1,2], Hiroshi Kimura[7.8], Takeshi Fukuma[1,2,9]*

[1] Nano Life Science Institute (WPI-NanoLSI), Kanazawa University, Kakuma-machi, Kanazawa, 920-1192, Japan
[2] Division of Electrical Engineering and Computer Science, Kanazawa University, Kakuma-machi, Kanazawa 920-1192, Japan
[3] Division of Tumor Cell Biology and Bioimaging, Cancer Research Institute of Kanazawa University, Kakuma-machi, Kanazawa 920-1192, Japan
[4] Department of Immunology, Kanazawa University Graduate School of Medical Sciences, Kakuma-machi, Kanazawa, Ishikawa, 920-1192, Japan
[5] Biochemistry and Molecular Biology, University of Maryland School of Medicine, 655 W. Baltimore Street, Baltimore, MD, 21201
[6] Division of Nano Life Science, Graduate School of Frontier Science Initiative, Kanazawa University, Kakuma-machi, Kanazawa 920-1192, Japan
[7] Cell Biology Center, Institute of Integrated Research, Institute of Science Tokyo, 4259 Nagatsuta-cho, Midori-ku, Yokohama, 226-8501, Japan
[8] Graduate School of Bioscience and Biotechnology, Institute of Science Tokyo, 4259 Nagatsuta-cho, Midori-ku, Yokohama, 226-8501, Japan
[9] Division of Nano Life Science, Kanazawa, University, 920-1192 Kanazawa, Japan
*Correspondence: tichikawa@staff.kanazawa-u.ac.jp

Abstract

During cancer invasion and metastasis, the mechanical properties of the nucleus change significantly, with reduced elasticity enhancing nuclear deformability to aid cell migration through tight spaces. Traditional methods of measuring nuclear elasticity, such as using bead-attached cantilevers on cells or isolated nuclei, are limited because they also measure the elasticity of surrounding structures, including cell membranes and cytoskeletons. In this study, we used a Nanoendoscopy-atomic force microscope (AFM) with a nanoneedle probe to directly measure nuclear elasticity in living cells. Our findings show that nuclear elasticity increases with serum depletion but decreases when serum-starved cells are treated with TGF-β, which induces epithelial-mesenchymal transition (EMT). In addition, trimethylation levels of histone H4 at lysine 20 but not the expression levels of nuclear lamins positively correlate with these nuclear elasticities. We propose that changes in nuclear elasticity during cancer progression are associated with alterations in chromatin structure (approximately 150 words).

Introduction

Cancer progression is accompanied by the remodeling of cell-cell and cell-extracellular matrix interactions, leading to the detachment of epithelial cells and promoting cell migration. This process is influenced by the mechanical properties of the cell, which result from the interactions between the nucleus, cytoskeleton, and plasma membrane[1-3]. Numerous studies have explored the link between cell mechanics and cancer metastasis[4-9]. Specifically, reduced nuclear elasticity enhances nuclear deformability, which facilitates the migration of cancer cells through tight spaces[10]. Supporting this, measurements of nuclear elasticity from breast, lung, thyroid, cervical, bladder, liver, and skin cancer cells often show that cancer cell nuclei are softer than those of normal cells[7,11-16]. However, some studies found stiffer nuclei in cancer cells from hepatocyte, cervical, and pancreatic tissues[13,17,18].

In mammalian cells, DNA wraps around histone octamers, forming nucleosome, which is further organized into a higher-order chromatin structure and enclosed by the nuclear envelope (NE). Chromatin can be divided into heterochromatin (tightly packed) and euchromatin (loosely packed)[19]. Heterochromatin is characterized by specific modifications, such as histone H3 lysine 9 dimethylation and trimethylation (H3K9me2 and H3K9me3, respectively), lysine 27 trimethylation (H3K27me3), and H4 lysine 20 trimethylation (H4K20me3), which mark transcriptionally inactive regions[20-23].

The NE consists of double phospholipid bilayers—the inner and outer nuclear membranes (INM and ONM)—and associated proteins[24]. A part of heterochromatin is anchored to the nuclear lamina (NL) lining the INM. The NL is connected to the

cytoskeletal system through the linker of the nucleoskeleton and cytoskeleton (LINC) complex, which is localized to the IMN and OMN and the lumen between them[25]. The major structural components of the NL are nuclear lamins, classified into A-type lamins (lamins A and C) and B-type lamins (lamins B1 and B2)[26,27]. These lamins assemble into a filament to form meshworks of the NL[28-31]. Both chromatin and the NL are the major determinants of nuclear mechanics.

Understanding nuclear mechanics can provide insights into for revealing how cells respond to different stresses. However, accurately measuring these properties has been challenging. Traditional methods using AFM with sharp or bead-attached cantilevers used to measure nuclear elasticity include cell membrane, cortical actin, and cytoplasmic filaments, and these components cannot be separated[9,32-40]. Another traditional method using AFM or micropipette aspiration on isolated nuclei may not reflect the natural state within living cells[9,32,33,39,41-46]. Additionally, methods using magnetic beads or optical tweezers cannot apply large forces and may not measure elasticity accurately[47,48].

Recent advances in AFM technology have shown that AFM with a nanoneedle probe can image intracellular structures at the nanoscale without affecting cell viability[49-51]. This technique, known as "Nanoendoscopy-AFM," enables for high-resolution observation of 3D structures such as actin fibers within living cells. In this study, we employed Nanoendoscopy-AFM to measure nuclear elasticity accurately in living cancer cells, focusing on differences between moderate and highly metastatic cells, and .

Results

Whole-cell measurement using Nanoendoscopy-AFM

Figure 1a illustrates the process of whole-cell measurement using 3D Nanoendoscopy-AFM. This technique involves repeatedly inserting a nanoneedle probe into the cell at various positions across the target area while performing force versus distance (F-z) curve measurements. The nanoneedle probe was fabricated by electron beam deposition (EBD) on the tip of a truncated commercial cantilever (BL-AC40TS-C2, spring constant: 0.1 N/m), as shown in Figure 1b. The 5 μm-length of the nanoneedle is long enough to measure the elasticity of the nuclear surface inside the living cell, and the diameter must be less than 200 nm because a thicker nanoneedle probe of more than 200 nm damages the cell[49].

Figure 1c presents a 3D reconstructed image of the entire cell, while Figure 1d depicts the cross-sectional force map along the plane A-B in Figure 1c and g. A typical F-z curve is displayed in Figure 1f, where "distance" refers to the distance from the dish surface to the cantilever tip, and "force" represents the force detected by the cantilever. The local rise around 5.7 μm from the dish surface in the force curve (right blue line part) indicates the initial contact point with the cell membrane (Cell CP), showing a plateau after membrane penetration. Another rise, at approximately 5 μm (left blue line part), marks the contact point with the nucleus (Nuclear CP). Figure 1e displays the cross-sectional fluorescence image at the Nuclear CP, which demonstrates the rise at Nuclear CP pushing the nuclear surface. By fitting the Herz-Sneddon model to each rise in the force curve, Young’s moduluses of the cell membrane and the nucleus can be measured separately [52].

By extracting data from Cell CP, we were able to reconstruct height and elasticity maps of the cell membrane (Figures 1g and 1h). Figure 1i presents a histogram of the cell membrane's Young's modulus (peak value: 2693 Pa). Similarly, data from Nuclear CP allowed us to reconstruct nuclear height and elasticity maps (Figures 1j and 1k), with Figure 1l showing Young's modulus histogram for the nucleus (peak value: 2972 Pa). Analyses were performed using custom software developed in-house[51].

Measurement of the nuclear elasticity of moderate and highly metastatic cells with and without serum

The previous studies have reported that euchromatin and heterochromatin levels modulate nuclear elasticity and that serum influences these chromatin states[53-55]. To investigate the effects of serum depletion on nuclear elasticity, we measured the elasticity of the intact nuclear surface in human lung cancer cells (PC9) [56]. Figure 2a illustrates the Nanoendoscopy-AFM method used for these measurement, where the nanoneedle probe scans specifically over the nuclear surface in 3D AFM mode. A height map of the nuclear surface (16 × 16 data over a 3 × 3 μm area) is shown in Figure 2b. Two distinct types of force curves were observed: one with a clear peak (Fig. 2c) and another without a distinct peak (Fig. 2d), likely due to failed penetration of the cell membrane by the nanoneedle tip. We selected 20 force curves exhibited clear peaks (Fig. 2c), and a fixed 100 pN range at the rise of the curve (blue line in Fig. 2c) was fitted to the Helz-Sneddon model. The indentation depth of the nucleus ranged from 150 to 250 nm, confirming that the measurement captured the elasticity of the NE and associated chromatin structures[57].

We measured the nuclear elasticity of living PC9 cells in culture media with and without serum. After two days of serum-free culture, nuclear elasticity significantly increased compared to conditions with serum (Fig. 2e-1 and Supplementary Table 1, $P < 0.0001$; with serum: 2714 ± 126 Pa (average ± SEM, N = 35); without serum: 4384 ± 284 Pa (N = 29)). We hypothesized that this increase in nuclear elasticity was due to changes in chromatin compaction. To test this, we measured levels of H4K20me3, a marker associated with chromatin compaction, via western blotting[46,54]. H4K20me3 levels were significantly increased under serum-depleted conditions compared to before the serum-depletion (Fig. 2f and g), indicating that serum depletion enhances chromatin compaction, leading to increased nuclear elasticity.

We performed similar experiments on brain-metastasized cells after heart injection (PC9-BrM)[58]. This higly metastasized cells may change the nuclear surface elasticity according to previous report[59]. Consistent with PC9 cells, serum depletion increased nuclear elasticity in PC9-BrM cells (Fig. 2e-2, $P < 0.0001$; with serum: 2394 ± 249 (N = 30); without serum: 4122 ± 269 (N = 30)) same as PC9. The H4K20me3 levels was also increased (Fig. 2f and g). Unexpectedly, no significant differences in nuclear elasticity were observed between PC9 and PC9-BrM cells, regardless of serum presence (Fig. 2e-3, $P = 0.47$; Fig. 2e-4, $P = 0.06$).

Figure 2h presents the results of cell membrane elasticity. In PC9 cells, cell membrane elasticity did not differ significantly between the presence and absence of serum (Fig, 2h-1, $P = 0.08$; with serum: 4722 ± 250 (N = 35); without serum: 4166 ± 198 (N = 31)). However, in PC9-BrM cells, cell membrane elasticity was significantly higher under serum-depleted conditions than normal serum-treated conditions (Fig, 2h-2, $P < 0.001$; with serum: 2929 ± 241 (N = 30); without serum: 6371 ± 477 (N = 27)). When comparing PC9 and PC9-BrM cells,

PC9-BrM cells exhibited lower cell membrane elasticity than PC9 cells in the presence of serum but higher elasticity under serum-free conditions (Fig. 2h-3 and Fig. 2h-4, $P < 0.001$). Increased expression levels of vimentin have been reported to enhance nuclear elasticity[60,61]. However, in serum-depleted conditions, vimentin expression was reduced (Fig. 2g). These results indicate that Nanoendoscopy-AFM successfully detects transitions in nuclear elasticity driven by changes in chromatin compaction caused by serum depletion, without interference from the cell membrane or cytoskeleton.

EMT induction using TGF-β and expression of lamins and histone modifications

Malignant transformation of cancer requires epithelial-mesenchymal transition (EMT) induction. To further investigate the relationship between metastasis and nuclear elasticity transitions, we examined wheter EMT induction altered nuclear elasticity. EMT was induced by adding transforming growth factor (TGF)-β to serum-free medium. EMT induction was confirmed by the upregulation of vimentin and N-cadherin (Fig. 3d and e). Nuclear elasticity significantly decreased following EMT induction compared to control cells (Fig. 3a, $P = 0.0018$; 3201 ± 197 Pa ($N = 30$)). In contrast, cell membrane elasticity remained unchanged (Fig. 3b, $P = 0.513$; 4097 ± 302 Pa ($N = 30$)). Figure 3c presents a representative nuclear elasticity map on a 1 × 1 μm scale, showing highly heterogeneous distributions of elasticity.

Previous studies have shown that the NL plays a crucial role in regulating nuclear elasticity[35,53,62-64]. To determine whether the expression levels of lamins (lamin A/C, B1, and B2) are affected by TGF-β treatment, we measured their expression levels by immunoblotting. As

shown in Figure 3d, the expression levels of lamin A/C, B1, and B2 remained unchanged between control (serum-depleted) and TGF-β treated cells. This suggest that lamins are not the primary factor regulating nuclear elasticity under these conditions. In contrast, H4K20me3 levels decreased in PC9 cells after EMT induction (Fig. 3d and e). These results support the hypothesis that chromatin compaction contributes to alterations in nuclear elasticity.

Measurement of cell adhesion area, nuclear volume, nuclear deformation

We investigated the effects of serum and TGF-β on cell spreading, nuclear volume, and nuclear deformation, as these factors may influence nuclear elasticity. Figure 4a shows fluorescence images of nuclei under serum treatment, serum depletion, and TGF-β treatment, while Figures 4d and 4e present the distribution of nuclear volume and circularity under each condition. The nuclear volume of serum-treated PC9 cells was significantly larger than that of serum-depleted cells. This increase in nuclear volume may reduce nuclear elasticity by lowering the concentration of structural components in the nuclear envelope. In contrast, there was no significant differences in nuclear volume between serum-depleted cells and TGF-β-treated cells. Circularity, calculated as $4\pi\times(\text{area}/\text{perimeter}^2)$, indicates how closely the shape resembles a perfect circle and serves as an indicator of nuclear deformation[65]. The results showed no significant differences in circularity under the three conditions. Figures 4d shows fluorescence images of the cells, and the quantified graph is presented in Figure 4e. The cell adhesion area was significantly reduced after serum depletion and increased following TGF-β treatment, likely due to enhanced lamellipodia spreading in response to serum and TGF-β.

Discussion

In this study, we have developed a novel method for measuring the nanoscale mechanical properties of nuclear elasticity in intact nuclei within living cancer cells using Nanoendoscopy-atomic force microscopy (Nanoendoscopy-AFM). Our findings demonstrate that nuclear elasticity decreases when cells cultured without serum are exposed to serum or TGF-β. Notably, we found no significant changes in the expression levels of lamins A/C, B1, and B2 under these conditions. However, we observe a significant increase in H4K20me3 levels. These findings strongly suggest that chromatin compaction states influence nuclear elasticity. Exposure to serum or TGF-β may reduce chromatin compaction, resulting in nuclear softening.

Comparisons between round and sharp tips for measuring cell membrane elasticity have been explored both experimentally and theoretically[66-69]. Since round tips are more influenced by the cytoskeletal system, which has elasticity values approximately an order of magnitude lower than the cell cortex, round tips tend to yield low elasticity values compared to sharp tips. For instance, studies using round tips have reported cell membrane elasticity values ranging from 0.2 to 2 kPa[14,66,67,69], while measurements using sharp tis ranged from 1.5 to 7 kPa[15,66,67,69]. In our experiments, the elasticity of lung cancer cell membrane ranged from 2 to 6 kPa, consistent with values obtained using sharp tips. The nanoneedle probe used in our study is significantly sharper than standard sharp tips, with an indentation depth of about 100 - 200 nm. This minimizes the influence of the cytoskeleton and enables more precise measurements of nuclear elasticity. For

the first time, we have measured intact nuclear elasticity in living cells using the nanoneedle probe.

We have also successfully mapped the elasticity distribution on the nuclear surface in living cells for the first time (Fig. 1k and Fig. 3c), which is only possible using Nanoendoscopy-AFM. With a tip diameter of 60 nm and an indentation depth of 100 - 200 nm, this probe detects elasticity within the ϕ60 and z100 - 200 nm space. The resulting elasticity map reveals highly heterogeneous distributions of nuclear elasticity. The nuclear lamina has a meshwork structure with a mesh size of 1 – 1.5 μm in diameter[28], and nuclear pore complexes (NPCs) are localized within these meshes[70]. Heterochromatin tethered to the nuclear lamina forms lamina-associated domains (LADs)[71], while regions near NPCs are enriched in euchromatin[30]. It is reasonable to speculate that these structural features contribute to the heterogeneous distributions of nuclear elasticity. Further experiments are required to elucidate the precise relationship between nuclear elasticity and these underlying structures. Our method offers enhanced precision for such investigations.

To date, no reports have examined the effect of serum and TGF-β on nuclear elasticity. We have demonstrated that nuclear elasticity decreases in the presence of serum compared to serum-free conditions in both moderate and highly metastatic cells. Because serum depletion increases H4K20me3 levels[55], these findings suggest that serum exposure reduces heterochromatin, which decreases nuclear elasticity, aligning with our results. Additionally, we have investigated the impact of TGF-β on nuclear elasticity in serum-free conditions and found that the TGF-β treatment reduces nuclear elasticity in both moderate and highly metastatic cells compared to serum-depleted cells without TGF-β treatment. Supporting

our findings, previous studies have reported that TGF-β decreases H4K20me3 levels[72] and triggers a widespread increase in chromatin accessibility[73]. These results strongly suggest that TGF-β promotes global chromatin relaxation, leading to a decrease in nuclear elasticity.

In comparing nuclear elasticity between moderate and highly metastatic cells, we have found that highly metastatic PC9 (PC-BrM) cells exhibit nuclear elasticity similar to that of moderate-metastatic PC9 cells. In contrast, the cell membrane elasticity of PC9 cells is significantly higher than the of PC-BrM cells in the presence of serum. Some previous studies reported that cancer cells have softer nuclei than normal cells, whereas others reported the opposite. These discrepancies may arise from limitations in prior methodologies, which often could not distinguish between cell membrane elasticity and nuclear elasticity. If nuclear elasticity is measured by indenting both the cell membrane and the nuclear in PC cells, it may be overestimated due to the contribution of the cell membrane. Similarly, another group has proposed that a decrease in nuclear elasticity in late-stage bladder cancer cells resulted from reduced expression of cytoskeletal proteins rather than changes in nuclear elasticity itself[33]. Although further studies across various cell types are needed, our results suggest that nuclear elasticity may remain unchanged even as cells acquire metastatic properties.

Measuring the mechanical properties of the nucleus has become a ‘gold standard’ for cancer diagnosis, making accurate nuclear elasticity measurement essential for precise clinical assessment[74,75]. The method developed in this study could serve as a fundamental technique in diagnostics and has broader applications for measuring the mechanical properties of other intracellular structures. The mechanical properties of structures within living cells remain largely unexplored, but our technique can be applied to measure the elasticity or adhesion properties of

other organelle structures, such as mitochondrial membranes or focal adhesions, in both normal and abnormal cells[76,77]. Understanding these mechanical properties will deepen our insights into nanoscale biology and the mechanisms underlying diseases associated with cellular dysfunctions [78].

Methods

Cell sample preparation

HeLa cells were obtained from the Japanese Collection of Research Bioresources (JCRB) Cell Bank (JCRB9004). PC9-Luc-EGFP and PC9-Luc-EGFP-BrM4 (brain-metastasized cells; referred to as PC9 and PC9-BrM, respectively, throughout the manuscript) were established in a previous study[58]. All cell lines were maintained in Dulbecco's Modified Eagle's Medium (DMEM, Gibco) supplemented with 10% fetal bovine serum (Biosera) and 1% penicillin/streptomycin (Fujifilm Wako).

Nanoendoscopy-AFM

PC9 and PC9-BrM cells were cultured on 35-mm plastic dishes in the DMEM (Fujifilm Wako) containing 10% serum, no serum, or no serum and 5 ng/ml TGF-β1 (Peprotech) for two days. Before observation, the culture medium was replaced with Leibovitz's L-15 medium (Thermo Fisher) supplemented with 1% penicillin/streptomycin and containing either 10% serum, no serum, or no serum with 5 ng/ml TGF-β1. All experiments were conducted within a few hours

after the medium change. The nuclear and cell membrane elasticities were measured using Nanoendoscopy-AFM methods[49-51]. Nanoneedle probes were fabricated using electron beam deposition with a focused ion beam system (Helios G4 CX Dual Beam) on tip-truncated cantilevers (Olympus, BLAC40TS-C2, spring constant approximately 0.1 N/m). We used a JPK NanoWizard 4 BioAFM (Bruker) equipped with an inverted fluorescence microscope (Eclipse Ti2, Nikon). The temperature was maintained at 37 °C using a dish heater (Bruker). Measurements were conducted in QI mode with the following parameters: 16 × 16 pixels, 5.5 μm Z-length, 1.5 nN setpoint, and 10 μm/s tip speed. 10 cells were measured per sample, and 20 force curves were recorded for each cell. Young's modulus was calculated by fitting the force carves within a fixed 0.1 nN range using the following equation with custom software[38]. F, Rc, and E, ν, δ indicate force, the probe's radius, Young's modulus, Poisson ratio, and indentation depth, respectively[51].

$$\boldsymbol{F = \frac{4\sqrt{R_c}}{3}\frac{E}{1-\nu^2}\delta^{3/2}}$$

Immunoblotting

Cultured cells on 10-cm dishes were washed three times with ice-cold PBS and lysed in 150 μl of RIPA or Laemmli buffer supplemented with protease inhibitor and phosphatase inhibitor cocktail (cOmplete and PhosSTOP, Roche). After lysis, samples were sonicated for two minutes, freeze-thaw once, and heated at 95°C for five minutes. Protein concentration was measured using a BCA Protein Assay Kit (BioDynamics Laboratory), and samples were adjusted to equal concentrations. Samples were mixed with 0.005% bromophenol blue (Nacalai) and 125 mM

DTT (Fujifilm Wako), then denatured at 95°C for five minutes. Proteins (3-20 μg) were separated on a 5-20% polyacrylamide gels (SuperSep Ace, Fujifilm Wako) and transferred onto a polyvinylidene fluoride (PVDF) or nitrocellulose membrane (Bio-Rad) using a Trans-Blot Turbo semi-dry transfer system (Bio-Rad). Membrane were blocked with Intercept Blocking Buffer (TBS; LI-COR) for one hour at room temperature, incubated overnight at 4°C with primary antibodies, and then incubated with secondary antibodies for one hour at room temperature. Antidodies used for immunoblotting are listed in Supplemental Table 4. Fluorescence signals were detected using an Odyssey CLx imaging system (LI-COR). Total proteins was visualized with Panceau S Staining Solution (Beacle), and images were analyzed using Image Studio Lite (LI-COR).

Measurement of cell area and nucleus volume

Cells are cultured on a glass-bottom dish (ibidi). For measuring nuclear volume and nuclear deformation, the nuclei were stained with 1 μM SiR-DNA (CY0SC007, Cytoskeleton). Fluorescence images were acquired in three dimensions using a confocal microscope (Abberior) with a resolution of 200 × 200 × 200 nm per pixel, using a 640 nm excitation and a 10 us exposure time. Image analysis was performed using a custom MATLAB script (R2024a, Simulink). For measuring cell adhesion area, the cytosol was stained with 1 μg/ml Calcein-AM (Dojindo), and the cell membrane was stained with PlasMem Bright Green (1:1000 dilution, Dojindo). Scatter plots were generated using Prism 9 (GraphPad Software).

Indirect immunofluorescence

Antibodies used for indirect immunofluorescence are listed in Table S1. Cells were cultured on 35-mm glass-based dishes (IWAKI) and fixed with 4% paraformaldehyde (Electron Microscopy Sciences) for 10 min, permeabilized with 0.1% Triton X-100 (Sigma-Aldrich) in PBS for 15 min, and then blocked with Blocking One-P (Nacalai Tesque) for 30 minutes. Fixed cells were incubated with primary antibody diluted in 10% Blocking One-P in PBS overnight at 4°C. The next day, cells were washed three times with 10% Blocking One-P in PBS and incubated with secondary antibodies in 10% Blocking One-P in PBS for one hour at room temperature. After washing with 10% Blocking One-P in PBS once, the cells were imaged with Abberior Expert Line (Abberior Instruments) equipped with an inverted microscope (IX83, Olympus). Acquired images were analyzed with ImageJ (NIH).

Statistical analyses

Welch's t tests were used for single comparisons, and Games-Howell tests were used for multiple comparisons, respectively, using EZR software (Saitama Medical Center, Jichi Medical University)[79].

Supplemental Information

Supplemental information can be found online at

Acknowledgments

This work was supported by World Premier International Research Center Initiative (WPI), MEXT, Japan, by JSPS KAKENHI under grant numbers 20H00345, 21H05251, 22H01954, and 23K05763. Ichikawa was supported by the Mitani Foundation for Research and Development, Takeda Science Foundation, Shimadzu Science Foundation, and Nakatani Foundation.

Author Contributions

T. I., Y. K., K. S., T. S. and T. F. designed the experiments. K. I. and E. H. prepared the cell lines. T. I. and K. S. performed the AFM experiment and analysis under the supervision of T. F.. Analysis software was developed by N. M. and T. M. under the supervision of K. M. and T. F.. A. K. and Y. K. performed immunoblotting under the supervision of K. I., E. H. and T. S.. H. K. produced mouse monoclonal anti-histone modification-specific antibodies. A. K. performed indirect immunofluorescence under the supervision of Y. K. and T. S.. T. Y. did preliminary analysis of the protein expression of the cell under the supervision of R. H.. T. I., Y. K. and T. S. wrote the manuscript. All authors read and approved the final manuscript.

Competing interests

The authors declare no competing interests.

Additional information

Supplementary information The online version contains

supplementary material available at

https://doi.org/.

Correspondence and requests for materials should be addressed to

Takehiko Ichikawa or Takeshi Fukuma.

Peer review information Nature Communications thanks Blaine Bartholomew and the other, anonymous, reviewer(s) for their contribution to the peer review of this work. A peer review file is available.

Reprints and permissions information is available at

http://www.nature.com/reprints

Publisher's note Springer Nature remains neutral with regard to jurisdictional claims in published maps and institutional affiliations.

Open Access

References

Figures

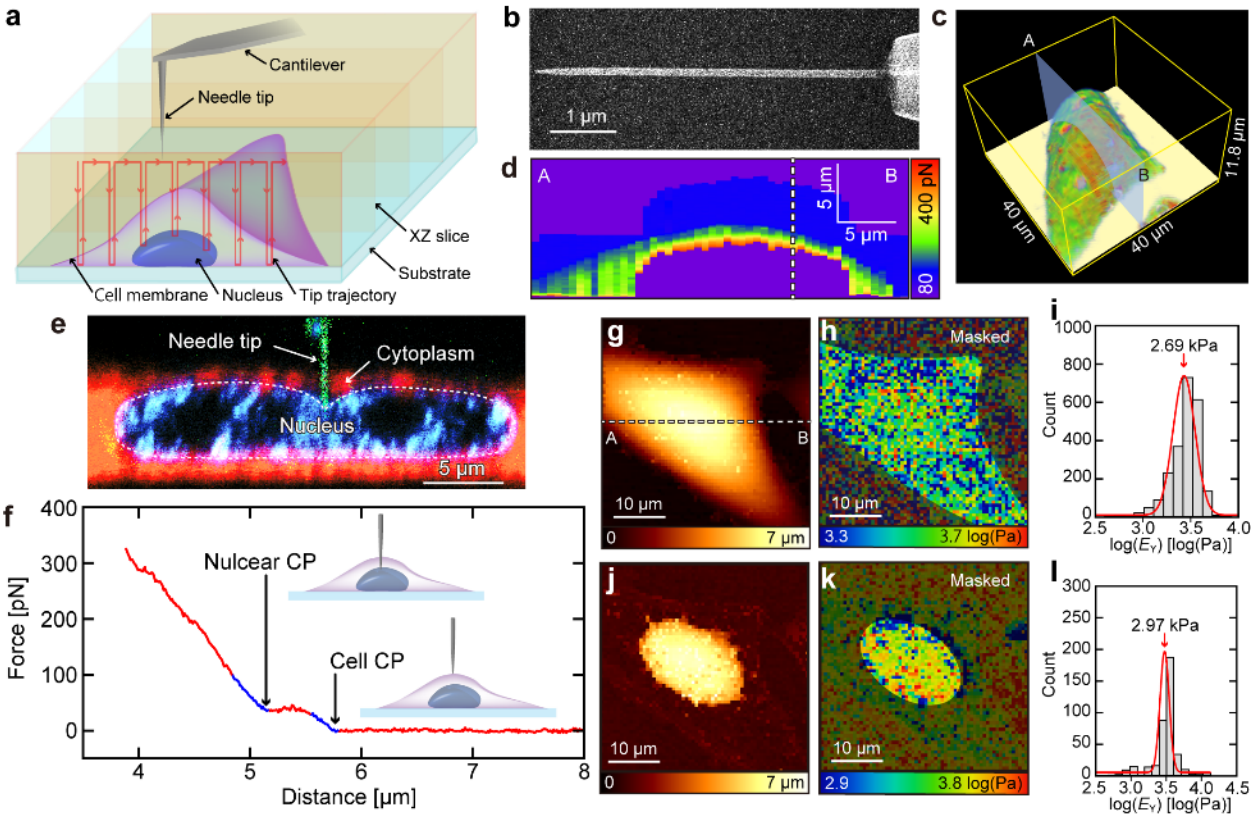

Figure 1. Nanoendoscopy-AFM measurement of a whole cell. (a) Schematic illustration of the Nanoendoscopy-AFM applied to a whole cell. (b) Scanning electron microscope image of nanoneedle probe. (c) Reconstructed 3D image of the cell membrane. (d) Cross-sectional force map along plane AB in panel (c). (e) Cross-section image showing the tip pressing against the nucleus. The nanoneedle probe, cytoplasm, and nucleus are stained green, red and blue, respectively. (f) Typical force-distance (F-z) curve during tip approach. The force represents the cantilever's detected force, while the distance indicates the tip's distance from the surfece of the dish. Cell contact point (Cell CP) and nuclear contact point (Nuclear CP) are marked. (g) Height map of the cell membrane. (h) Young's modulus map of the cell membrane. (i) Histogram of Young's modulus values for the cell membrane (peak value 2.69 kPa). (j) Height map of the nucleus. (k) Young's modulus map of the nuclear surface. (l) Histogram of the Young's modulus values for the nuclear surface (peak value 3.00 kPa).

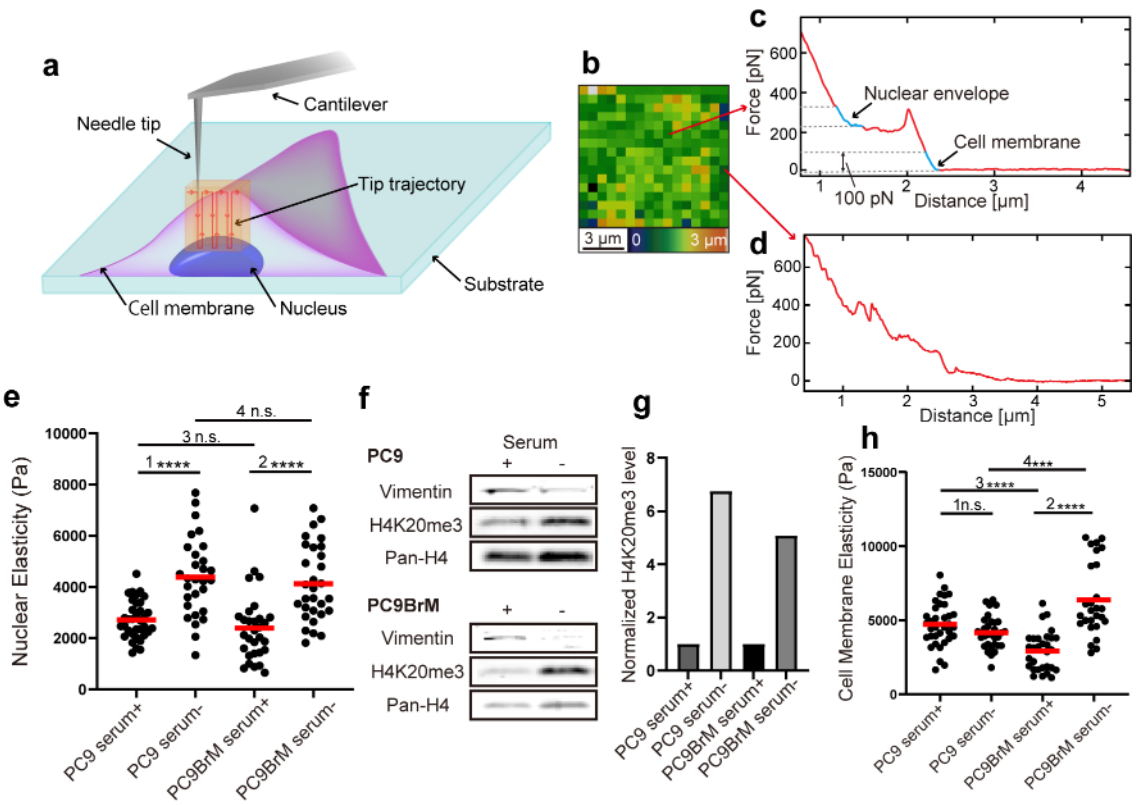

Figure 2. Nanoendoscopy-AFM measurement of the nucleus. (a) Schematic illustration of Nanoendoscopy-AFM for measuring the nuclear surface. (b) Height map of the nucleus. (c) Force curve showing clear penetration of the cell membrane. (d) Force curve without penetration. (e) Distribution of nuclear elasticity of PC9 and PC9-BrM4 cells uder normal (serum+) and serum-depletion (serum-). Statistical significance is indicated as follows: **** P < 0.0001, n.s. (non-significant). (f) Distribution of cell membrane elasticity in PC9 and PC9-BrM cells under serum+ and serum-. Statistical significance *** indicates P < 0.001. (g) Representative expression levels of vimentin, H4K20me3 and pan-H4in PC9 and PC9-BrM with and without serum. (h) Bar graph of quantified levels of H4K20me3 normalized to pan-H4 from (g) by densitometry. Each bar was normalized to the expression level under serum+ conditions in PC9 and PC9BrM, respectively.

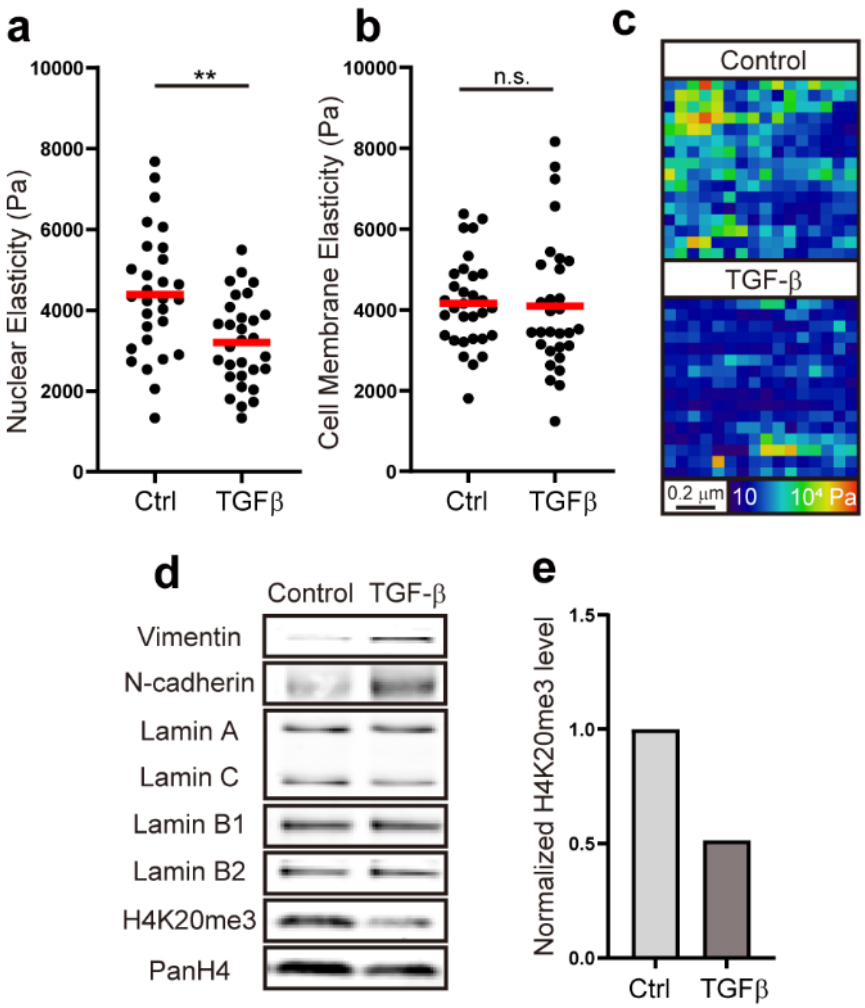

Figure 3. Measurement of the effect of EMT induction by TGF-β on nuclear and cell elasticity, as well as on lamins and histone modifications. (a) Nuclear elasticity of control (serum-free) and TGF-β treated cells. Statistical significance (**) indicates $P < 0.01$. (b) Cell membrane elasticity. (c) Representative elasticity map of control and TGF-β treated cell nuclear surface. (d) Representative expression levels of EMT markers (vimentin and N-cadherin), lamins, H4K20me3, and pan-H4. (e) Densitometrically quantified graph of H4K20me3 normalized to pan-H4 from (d).

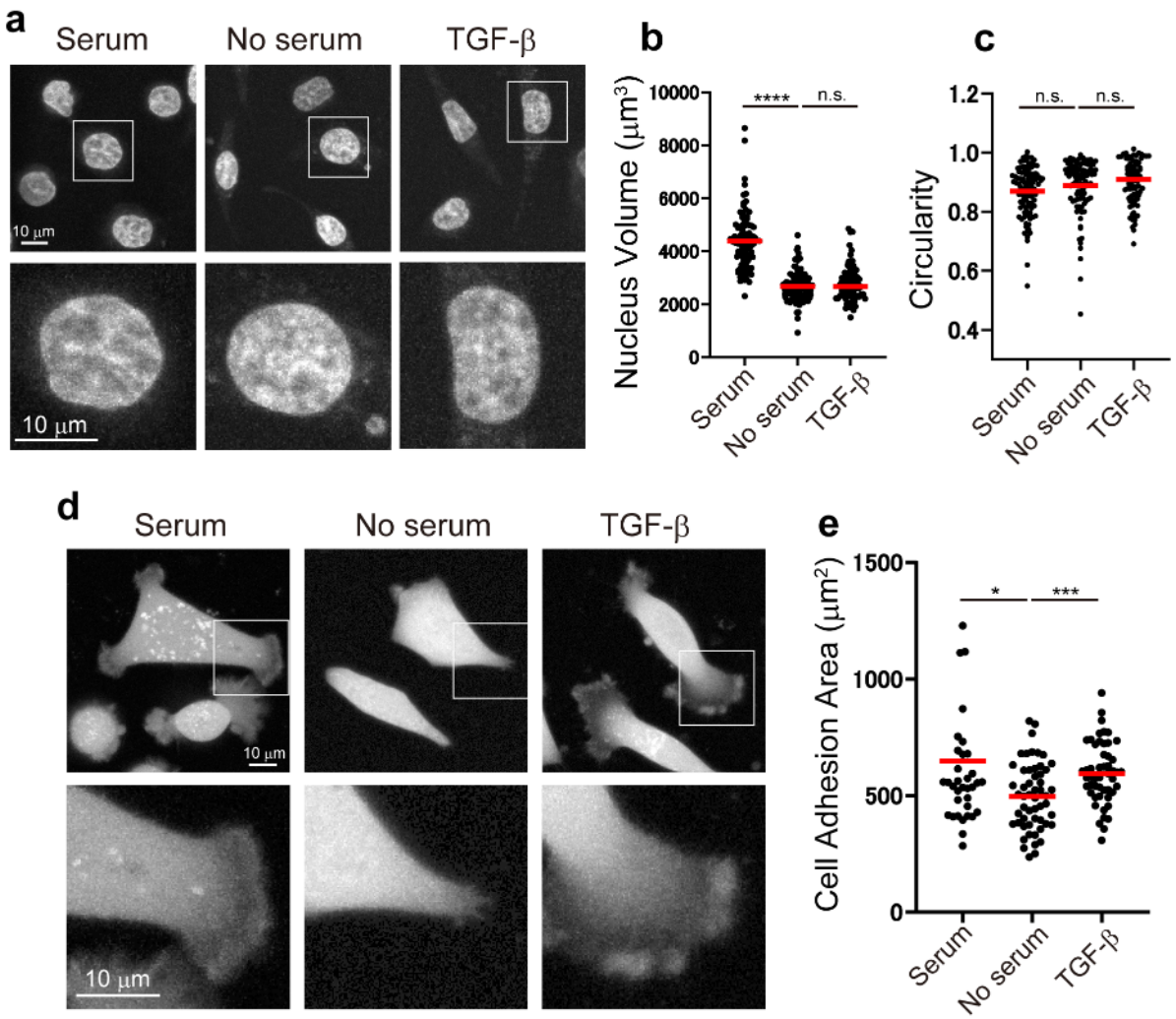

Figure 4. Quantification of nuclear volume, nuclear deformation, and cell adhesion area under serum, serum depletion, and TGF-β treatment. (a) Representative fluorescence images of nuclei for each treatment condition are shown as maximum-intensity projections. The images in the bottom row are magnified views of white boxes. (b) Distribution of nuclear volume. Statistical significance is indicated as follows: **** $P < 0.0001$ and n.s. (non-significant). (c) Distribution of the nuclear circularity. (d) Representative fluorescence images of nuclei under serum-containing medium, serum depletion, and TGF-β treatment. (e) Distribution of cell adhesion area. Statistical significance is indicated as follows: *** $P < 0.001$, * $P < 0.05$.

1 Dongre, A. & Weinberg, R. A. New insights into the mechanisms of epithelial-mesenchymal transition and implications for cancer. *Nat Rev Mol Cell Biol* **20**, 69-84 (2019). https://doi.org:10.1038/s41580-018-0080-4

2 Leggett, S. E., Hruska, A. M., Guo, M. & Wong, I. Y. The epithelial-mesenchymal transition and the cytoskeleton in bioengineered systems. *Cell Commun Signal* **19**, 32 (2021). https://doi.org:10.1186/s12964-021-00713-2

3 Leggett, S. E. *et al.* Morphological single cell profiling of the epithelial-mesenchymal transition. *Integr Biol (Camb)* **8**, 1133-1144 (2016). https://doi.org:10.1039/c6ib00139d

4 Coceano, G. *et al.* Investigation into local cell mechanics by atomic force microscopy mapping and optical tweezer vertical indentation. *Nanotechnology* **27**, 065102 (2016). https://doi.org:10.1088/0957-4484/27/6/065102

5 Faria, E. C. *et al.* Measurement of elastic properties of prostate cancer cells using AFM. *Analyst* **133**, 1498-1500 (2008). https://doi.org:10.1039/b803355b

6 Lekka, M. *et al.* Cancer cell detection in tissue sections using AFM. *Arch Biochem Biophys* **518**, 151-156 (2012). https://doi.org:10.1016/j.abb.2011.12.013

7 Lekka, M. *et al.* Elasticity of normal and cancerous human bladder cells studied by scanning force microscopy. *Eur Biophys J* **28**, 312-316 (1999). https://doi.org:10.1007/s002490050213

8 Rebelo, L. M., de Sousa, J. S., Mendes Filho, J. & Radmacher, M. Comparison of the viscoelastic properties of cells from different kidney cancer phenotypes measured with atomic force microscopy. *Nanotechnology* **24**, 055102 (2013). https://doi.org:10.1088/0957-4484/24/5/055102

9 Fischer, T., Hayn, A. & Mierke, C. T. Effect of Nuclear Stiffness on Cell Mechanics and Migration of Human Breast Cancer Cells. *Front Cell Dev Biol* **8**, 393 (2020). https://doi.org:10.3389/fcell.2020.00393

10 Liu, Z. *et al.* Cancer cells display increased migration and deformability in pace with metastatic progression. *FASEB J* **34**, 9307-9315 (2020). https://doi.org:10.1096/fj.202000101RR

11 Xie, Y., Wang, M., Cheng, M., Gao, Z. & Wang, G. The viscoelastic behaviors of several kinds of cancer cells and normal cells. *J Mech Behav Biomed Mater* **91**, 54-58 (2019). https://doi.org:10.1016/j.jmbbm.2018.11.029

12 Zhao, X., Zhong, Y., Ye, T., Wang, D. & Mao, B. Discrimination Between Cervical Cancer Cells and Normal Cervical Cells Based on Longitudinal Elasticity Using Atomic Force Microscopy. *Nanoscale Res Lett* **10**, 482 (2015). https://doi.org:10.1186/s11671-015-1174-y

13 Cross, S. E., Jin, Y. S., Rao, J. & Gimzewski, J. K. Nanomechanical analysis of cells from cancer patients. *Nat Nanotechnol* **2**, 780-783 (2007). https://doi.org:10.1038/nnano.2007.388

14 Li, Q. S., Lee, G. Y., Ong, C. N. & Lim, C. T. AFM indentation study of breast cancer cells. *Biochem Biophys Res Commun* **374**, 609-613 (2008). https://doi.org:10.1016/j.bbrc.2008.07.078

15 Rianna, C. & Radmacher, M. Comparison of viscoelastic properties of cancer and normal thyroid cells on different stiffness substrates. *Eur Biophys J* **46**, 309-324 (2017). https://doi.org:10.1007/s00249-016-1168-4

16 Liu, H. *et al.* In situ mechanical characterization of the cell nucleus by atomic force microscopy. *ACS Nano* **8**, 3821-3828 (2014). https://doi.org:10.1021/nn500553z

17 Zhang, G., Long, M., Wu, Z. Z. & Yu, W. Q. Mechanical properties of hepatocellular carcinoma cells. *World J Gastroenterol* **8**, 243-246 (2002). https://doi.org:10.3748/wjg.v8.i2.243

18 Iyer, S., Gaikwad, R. M., Subba-Rao, V., Woodworth, C. D. & Sokolov, I. Atomic force microscopy detects differences in the surface brush of normal and cancerous cells. *Nat Nanotechnol* **4**, 389-393 (2009). https://doi.org:10.1038/nnano.2009.77

19 Gilbert, N. *et al.* Chromatin architecture of the human genome: gene-rich domains are enriched in open chromatin fibers. *Cell* **118**, 555-566 (2004). https://doi.org:10.1016/j.cell.2004.08.011

20 Allshire, R. C. & Madhani, H. D. Ten principles of heterochromatin formation and function. *Nat Rev Mol Cell Biol* **19**, 229-244 (2018). https://doi.org:10.1038/nrm.2017.119

21 Tian, H. *et al.* PHF14 enhances DNA methylation of SMAD7 gene to promote TGF-beta-driven lung adenocarcinoma metastasis. *Cell Discov* **9**, 41 (2023). https://doi.org:10.1038/s41421-023-00528-0

22 Zhang, H. J. *et al.* Transforming growth factor-beta1 promotes lung adenocarcinoma invasion and metastasis by epithelial-to-mesenchymal transition. *Mol Cell Biochem* **355**, 309-314 (2011). https://doi.org:10.1007/s11010-011-0869-3

23 Zhang, N. *et al.* Decitabine reverses TGF-beta1-induced epithelial-mesenchymal transition in non-small-cell lung cancer by regulating miR-200/ZEB axis. *Drug Des Devel Ther* **11**, 969-983 (2017). https://doi.org:10.2147/DDDT.S129305

24 Ungricht, R. & Kutay, U. Mechanisms and functions of nuclear envelope remodelling. *Nat Rev Mol Cell Biol* **18**, 229-245 (2017). https://doi.org:10.1038/nrm.2016.153

25 Crisp, M. *et al.* Coupling of the nucleus and cytoplasm: role of the LINC complex. *J Cell Biol* **172**, 41-53 (2006). https://doi.org:10.1083/jcb.200509124

26 Gerace, L. & Blobel, G. The nuclear envelope lamina is reversibly depolymerized during mitosis. *Cell* **19**, 277-287 (1980). https://doi.org:10.1016/0092-8674(80)90409-2

27 Foisner, R. & Gerace, L. Integral membrane proteins of the nuclear envelope interact with lamins and chromosomes, and binding is modulated by mitotic phosphorylation. *Cell* **73**, 1267-1279 (1993). https://doi.org:10.1016/0092-8674(93)90355-t

28 Shimi, T. *et al.* Structural organization of nuclear lamins A, C, B1, and B2 revealed by superresolution microscopy. *Mol Biol Cell* **26**, 4075-4086 (2015).

https://doi.org:10.1091/mbc.E15-07-0461

29 Shimi, T. *et al.* The A- and B-type nuclear lamin networks: microdomains involved in chromatin organization and transcription. *Genes Dev* **22**, 3409-3421 (2008). https://doi.org:10.1101/gad.1735208

30 Schermelleh, L. *et al.* Subdiffraction multicolor imaging of the nuclear periphery with 3D structured illumination microscopy. *Science* **320**, 1332-1336 (2008). https://doi.org:10.1126/science.1156947

31 Turgay, Y. *et al.* The molecular architecture of lamins in somatic cells. *Nature* **543**, 261-264 (2017). https://doi.org:10.1038/nature21382

32 Wang, S. Q. *et al.* Membrane Deformability and Membrane Tension of Single Isolated Mitochondria. *Cell Mol Bioeng* **1**, 67-74 (2008). https://doi.org:10.1007/s12195-008-0002-1

33 Wang, X. *et al.* Mechanical stability of the cell nucleus - roles played by the cytoskeleton in nuclear deformation and strain recovery. *J Cell Sci* **131** (2018). https://doi.org:10.1242/jcs.209627

34 Krause, M., Te Riet, J. & Wolf, K. Probing the compressibility of tumor cell nuclei by combined atomic force-confocal microscopy. *Phys Biol* **10**, 065002 (2013). https://doi.org:10.1088/1478-3975/10/6/065002

35 Swift, J. *et al.* Nuclear lamin-A scales with tissue stiffness and enhances matrix-directed differentiation. *Science* **341**, 1240104 (2013). https://doi.org:10.1126/science.1240104

36 Hobson, C. M. *et al.* Correlating nuclear morphology and external force with combined atomic force microscopy and light sheet imaging separates roles of chromatin and lamin A/C in nuclear mechanics. *Mol Biol Cell* **31**, 1788-1801 (2020). https://doi.org:10.1091/mbc.E20-01-0073

37 Lanzicher, T. *et al.* AFM single-cell force spectroscopy links altered nuclear and cytoskeletal mechanics to defective cell adhesion in cardiac myocytes with a nuclear lamin mutation. *Nucleus-Phila* **6**, 394-407 (2015). https://doi.org:10.1080/19491034.2015.1084453

38 Vinckier, A. & Semenza, G. Measuring elasticity of biological materials by atomic force microscopy. *FEBS Lett* **430**, 12-16 (1998). https://doi.org:10.1016/s0014-5793(98)00592-4

39 Wang, K., Qin, Y. & Chen, Y. In situ AFM detection of the stiffness of the in situ exposed cell nucleus. *Biochim Biophys Acta Mol Cell Res* **1868**, 118985 (2021). https://doi.org:10.1016/j.bbamcr.2021.118985

40 Beicker, K., O'Brien, E. T., 3rd, Falvo, M. R. & Superfine, R. Vertical Light Sheet Enhanced Side-View Imaging for AFM Cell Mechanics Studies. *Sci Rep* **8**, 1504 (2018). https://doi.org:10.1038/s41598-018-19791-3

41 Wei, F., Lan, F., Liu, B., Liu, L. Q. & Li, G. Y. Poroelasticity of cell nuclei revealed through atomic force microscopy characterization. *Appl Phys Lett* **109** (2016). https://doi.org:Artn 213701 10.1063/1.4968191

42 Zhou, G. Q., Zhang, B. K., Tang, G. L., Yu, X. F. & Galluzzi, M. Cells nanomechanics by atomic force microscopy: focus on interactions at nanoscale. *Adv Phys-X* **6** (2021). https://doi.org:Artn

1866668
10.1080/23746149.2020.1866668

43 Ujihara, Y., Ono, D., Ito, M., Sugita, S. & Nakamura, M. Nuclear deformability of cancer cells with different metastatic potential. *Journal of Biorheology* **37**, 56-63 (2023).

44 Rowat, A. C., Lammerding, J. & Ipsen, J. H. Mechanical properties of the cell nucleus and the effect of emerin deficiency. *Biophys J* **91**, 4649-4664 (2006). https://doi.org:10.1529/biophysj.106.086454

45 Dahl, K. N., Kahn, S. M., Wilson, K. L. & Discher, D. E. The nuclear envelope lamina network has elasticity and a compressibility limit suggestive of a molecular shock absorber. *J Cell Sci* **117**, 4779-4786 (2004). https://doi.org:10.1242/jcs.01357

46 Pajerowski, J. D., Dahl, K. N., Zhong, F. L., Sammak, P. J. & Discher, D. E. Physical plasticity of the nucleus in stem cell differentiation. *Proc Natl Acad Sci U S A* **104**, 15619-15624 (2007). https://doi.org:10.1073/pnas.0702576104

47 Tang, W. *et al.* Indentation induces instantaneous nuclear stiffening and unfolding of nuclear envelope wrinkles. *Proc Natl Acad Sci U S A* **120**, e2307356120 (2023). https://doi.org:10.1073/pnas.2307356120

48 Mazumder, A., Roopa, T., Basu, A., Mahadevan, L. & Shivashankar, G. V. Dynamics of chromatin decondensation reveals the structural integrity of a mechanically prestressed nucleus. *Biophys J* **95**, 3028-3035 (2008). https://doi.org:10.1529/biophysj.108.132274

49 Penedo, M. *et al.* Visualizing intracellular nanostructures of living cells by nanoendoscopy-AFM. *Sci Adv* **7**, eabj4990 (2021). https://doi.org:10.1126/sciadv.abj4990

50 Penedo, M. *et al.* Cell penetration efficiency analysis of different atomic force microscopy nanoneedles into living cells. *Sci Rep* **11**, 7756 (2021). https://doi.org:10.1038/s41598-021-87319-3

51 Ichikawa, T. *et al.* Protocol for live imaging of intracellular nanoscale structures using atomic force microscopy with nanoneedle probes. *STAR Protoc* **4**, 102468 (2023). https://doi.org:10.1016/j.xpro.2023.102468

52 Sneddon, I. N. The relation between load and penetration in the axisymmetric Boussinesq problem for a punch of arbitrary profile. *International journal of engineering science* **3**, 47-57 (1965).

53 Stephens, A. D., Banigan, E. J., Adam, S. A., Goldman, R. D. & Marko, J. F. Chromatin and lamin A determine two different mechanical response regimes of the cell nucleus. *Mol Biol Cell* **28**, 1984-1996 (2017). https://doi.org:10.1091/mbc.E16-09-0653

54 Stephens, A. D. *et al.* Chromatin histone modifications and rigidity affect nuclear morphology independent of lamins. *Mol Biol Cell* **29**, 220-233 (2018). https://doi.org:10.1091/mbc.E17-06-0410

55 Kourmouli, N. *et al.* Heterochromatin and tri-methylated lysine 20 of histone H4 in animals. *J Cell*

Sci **117**, 2491-2501 (2004). https://doi.org:10.1242/jcs.01238

56 Kinjo, M. *et al.* Thromboplastic and fibrinolytic activities of cultured human cancer cell lines. *Br J Cancer* **39**, 15-23 (1979). https://doi.org:10.1038/bjc.1979.3

57 Allen, T. D. *et al.* Scanning electron microscopy of nuclear structure. *Methods Cell Biol* **88**, 389-409 (2008). https://doi.org:10.1016/S0091-679X(08)00420-2

58 Hirata, E. *et al.* The Brain Microenvironment Induces DNMT1 Suppression and Indolence of Metastatic Cancer Cells. *iScience* **23**, 101480 (2020). https://doi.org:10.1016/j.isci.2020.101480

59 Kwon, S., Yang, W., Moon, D. & Kim, K. S. Comparison of Cancer Cell Elasticity by Cell Type. *J Cancer* **11**, 5403-5412 (2020). https://doi.org:10.7150/jca.45897

60 Patteson, A. E. *et al.* Vimentin protects cells against nuclear rupture and DNA damage during migration. *J Cell Biol* **218**, 4079-4092 (2019). https://doi.org:10.1083/jcb.201902046

61 Pogoda, K. *et al.* Unique Role of Vimentin Networks in Compression Stiffening of Cells and Protection of Nuclei from Compressive Stress. *Nano Lett* **22**, 4725-4732 (2022). https://doi.org:10.1021/acs.nanolett.2c00736

62 Broers, J. L. *et al.* Decreased mechanical stiffness in LMNA-/- cells is caused by defective nucleo-cytoskeletal integrity: implications for the development of laminopathies. *Hum Mol Genet* **13**, 2567-2580 (2004). https://doi.org:10.1093/hmg/ddh295

63 Lammerding, J. *et al.* Lamins A and C but not lamin B1 regulate nuclear mechanics. *J Biol Chem* **281**, 25768-25780 (2006). https://doi.org:10.1074/jbc.M513511200

64 Ovsiannikova, N. L. *et al.* Lamin A as a Determinant of Mechanical Properties of the Cell Nucleus in Health and Disease. *Biochemistry (Mosc)* **86**, 1288-1300 (2021). https://doi.org:10.1134/S0006297921100102

65 Kamikawa, Y. *et al.* Impact of cell cycle on repair of ruptured nuclear envelope and sensitivity to nuclear envelope stress in glioblastoma. *Cell Death Discov* **9**, 233 (2023). https://doi.org:10.1038/s41420-023-01534-7

66 Guz, N., Dokukin, M., Kalaparthi, V. & Sokolov, I. If cell mechanics can be described by elastic modulus: study of different models and probes used in indentation experiments. *Biophys J* **107**, 564-575 (2014). https://doi.org:10.1016/j.bpj.2014.06.033

67 Vahabikashi, A. *et al.* Probe Sensitivity to Cortical versus Intracellular Cytoskeletal Network Stiffness. *Biophys J* **116**, 518-529 (2019). https://doi.org:10.1016/j.bpj.2018.12.021

68 Park, S., Duong, C. T., Lee, J. H., Lee, S. S. & Son, K. Effect of Tip Geometry of Atomic Force Microscope on Mechanical Responses of Bovine Articular Cartilage and Agarose Gel. *Int J Precis Eng Man* **11**, 129-136 (2010). https://doi.org:10.1007/s12541-010-0016-1

69 Vargas-Pinto, R., Gong, H., Vahabikashi, A. & Johnson, M. The effect of the endothelial cell cortex on atomic force microscopy measurements. *Biophys J* **105**, 300-309 (2013). https://doi.org:10.1016/j.bpj.2013.05.034

70 Shevelyov, Y. Y. Interactions of Chromatin with the Nuclear Lamina and Nuclear Pore Complexes. *Int J Mol Sci* **24** (2023). https://doi.org:10.3390/ijms242115771

71 Guelen, L. *et al.* Domain organization of human chromosomes revealed by mapping of nuclear lamina interactions. *Nature* **453**, 948-951 (2008). https://doi.org:10.1038/nature06947

72 Lyu, G. *et al.* Addendum: TGF-beta signaling alters H4K20me3 status via miR-29 and contributes to cellular senescence and cardiac aging. *Nat Commun* **9**, 4134 (2018). https://doi.org:10.1038/s41467-018-06710-3

73 Guerrero-Martinez, J. A., Ceballos-Chavez, M., Koehler, F., Peiro, S. & Reyes, J. C. TGFbeta promotes widespread enhancer chromatin opening and operates on genomic regulatory domains. *Nat Commun* **11**, 6196 (2020). https://doi.org:10.1038/s41467-020-19877-5

74 Liu, S. *et al.* Mechanotherapy in oncology: Targeting nuclear mechanics and mechanotransduction. *Adv Drug Deliv Rev* **194**, 114722 (2023). https://doi.org:10.1016/j.addr.2023.114722

75 Xu, W. *et al.* Cell stiffness is a biomarker of the metastatic potential of ovarian cancer cells. *PLoS One* **7**, e46609 (2012). https://doi.org:10.1371/journal.pone.0046609

76 Feng, Q. & Kornmann, B. Mechanical forces on cellular organelles. *J Cell Sci* **131** (2018). https://doi.org:10.1242/jcs.218479

77 Bartolak-Suki, E., Imsirovic, J., Nishibori, Y., Krishnan, R. & Suki, B. Regulation of Mitochondrial Structure and Dynamics by the Cytoskeleton and Mechanical Factors. *Int J Mol Sci* **18** (2017). https://doi.org:10.3390/ijms18081812

78 Meyers, M. A., Chen, P. Y., Lopez, M. I., Seki, Y. & Lin, A. Y. Biological materials: a materials science approach. *J Mech Behav Biomed Mater* **4**, 626-657 (2011). https://doi.org:10.1016/j.jmbbm.2010.08.005

79 Kanda, Y. Investigation of the freely available easy-to-use software 'EZR' for medical statistics. *Bone Marrow Transplant* **48**, 452-458 (2013). https://doi.org:10.1038/bmt.2012.244